PHYSICAL REVIEW E **66**, 051303 (2002)

Molecular dynamics simulations of vibrated granular gases

Alain Barrat* and Emmanuel Trizac†
Laboratoire de Physique Théorique (UMR 8627 du CNRS), Bâtiment 210, Université de Paris–Sud, 91405 Orsay Cedex, France
(Received 10 July 2002; published 18 November 2002)

We present molecular dynamics simulations of monodisperse or bidisperse inelastic granular gases driven by vibrating walls, in two dimensions (without gravity). Because of the energy injection at the boundaries, a situation often met experimentally, density and temperature fields display heterogeneous profiles in the direction perpendicular to the walls. A general equation of state for an arbitrary mixture of fluidized inelastic hard spheres is derived and successfully tested against numerical data. Single-particle velocity distribution functions with non-Gaussian features are also obtained, and the influence of various parameters (inelasticity coefficients, density, etc.) are analyzed. The validity of a recently proposed random restitution coefficient model is assessed through the study of projected collisions onto the direction perpendicular to that of energy injection. For the binary mixture, the nonequipartition of translational kinetic energy is studied and compared both to experimental data and to the case of homogeneous energy injection (''stochastic thermostat''). The rescaled velocity distribution functions are found to be very similar for both species.

DOI: 10.1103/PhysRevE.66.051303 PACS number(s): 81.05.Rm, 45.70.Mg, 45.70.−n, 51.10.+y

I. INTRODUCTION

Due to the intrinsic dissipative character of interparticle collisions, an energy supply is requested to fluidize a granular gas. This is often achieved by a vibrating boundary, and the resulting vibrofluidized beds provide nontrivial realizations of nonequilibrium steady states. The understanding of such far from equilibrium systems requires a correct description of the energy exchange between the vibrating piston and the granular medium, as well as a macroscopic continuum theory to describe the evolution of the relevant coarse-grained fields [1–3] (density, temperature, etc.). In particular, the derivation of an accurate equation of state is a key step in the hydrodynamic approach.

A simple, fair, and much studied theoretical framework to capture the inelastic nature of grain-grain collisions in a rapid granular flow is provided by the inelastic hard sphere model [4,5]. In this paper, we present the results of extensive molecular dynamics (MD) simulations of inelastic hard spheres driven by an energy injection at the boundaries, for both a one-component fluid (monodisperse case) and a binary mixture (bidisperse situation). We analyze in detail the effects of several parameters that may be difficult to tune experimentally, with a particular emphasis on the profiles of the hydrodynamic fields.

This paper is organized as follows. In Sec. II, we present the model and derive an equation of state for an arbitrary mixture of inelastic hard spheres, going beyond the ideal gas contribution in view of performing accurate hydrodynamic tests. The equation of state obtained is a natural generalization of its standard counterpart for elastic hard spheres. The following two sections (Secs. III and IV) are then devoted to molecular dynamics simulations for one-component systems and for binary mixtures. In both cases, we restrict ourselves to two-dimensional simulations, both for simplicity and for comparisons with two-dimensional (2D) experimental data [6–9]. As in the experiments, the energy loss due to inelastic collisions is compensated for by an energy injection by vibrating or thermal walls, which leads to heterogeneous density and temperature profiles. The various profiles and velocity distribution functions are studied and compared with experiments whenever possible. Moreover, projecting the dynamics onto the direction perpendicular to that of energy injection allows one to assess the validity of the random restitution coefficient model proposed in Refs. [10,11]. The influence of various parameters on the nonequipartition of energy in a binary mixture is studied in Sec. IV, and comparison with experimental data and with the case of homogeneous energy injection is performed. In this latter case, the velocity distribution functions are analyzed and shown to be very similar for the two species. Conclusions are finally presented in Sec. V.

II. THE MODEL—COMPUTATION OF AN EQUATION OF STATE

We consider a mixture of $\mathcal{N}_s$ species of hard spheres in dimension d, with diameters σ_i and masses m_i, where $1 \leqslant i \leqslant \mathcal{N}_s$. A binary collision between grains of species i and j is momentum conserving and dissipates kinetic energy. In the simplest version of the model, the collision i-j is characterized by one inelasticity parameter: the coefficient of normal restitution α_{ij}. Accordingly, the precollisional velocities $(\boldsymbol{v}_i, \boldsymbol{v}_j)$ are transformed into the postcollisional couple $(\boldsymbol{v}_i', \boldsymbol{v}_j')$, such that

$$\boldsymbol{v}_i' = \boldsymbol{v}_i - \frac{m_j}{m_i + m_j}(1+\alpha_{ij})(\hat{\boldsymbol{\sigma}}\cdot\boldsymbol{v}_{ij})\hat{\boldsymbol{\sigma}}, \tag{1}$$

$$\boldsymbol{v}_j' = \boldsymbol{v}_j + \frac{m_i}{m_i + m_j}(1+\alpha_{ij})(\hat{\boldsymbol{\sigma}}\cdot\boldsymbol{v}_{ij})\hat{\boldsymbol{\sigma}}, \tag{2}$$

*Electronic address: Alain.Barrat@th.u-psud.fr
†Electronic address: Emmanuel.Trizac@th.u-psud.fr

where $\boldsymbol{v}_{ij}=\boldsymbol{v}_i-\boldsymbol{v}_j$ and $\hat{\boldsymbol{\sigma}}$ is the center-to-center unit vector from particle i to particle j. Note that $\alpha_{ij}=\alpha_{ji}$ to ensure the conservation of total linear momentum $m_i\boldsymbol{v}_i+m_j\boldsymbol{v}_j$.

We also considered an extension of the previous model allowing for rotations, introducing a coefficient of tangential restitution $(\alpha_{ij}^t)\in[-1;1]$ [12], see Appendix A: the collision law for smooth spheres (1), (2) is then recovered for $\alpha_{ij}^t=-1$, while complete reversal of the tangential component of the relative velocity is obtained for $\alpha_{ij}^t=1$. Values in between correspond to a decrease of the absolute value of the tangential relative velocity, with reversal for $\alpha_{ij}^t>0$ and without for $\alpha_{ij}^t<0$.

Irrespective of the value of the tangential restitution coefficient α^t, the linear-momentum change for particle i in a collision i-j reads

$$\delta\boldsymbol{p}_i=-\delta\boldsymbol{p}_j=-\frac{m_im_j}{m_i+m_j}(1+\alpha_{ij})(\hat{\boldsymbol{\sigma}}\cdot\boldsymbol{v}_{ij})\hat{\boldsymbol{\sigma}}. \tag{3}$$

In Appendix B, we use this relation to compute an equation of state for the homogeneous isotropic mixture, invoking the virial theorem (the pressure is defined kinetically from the momentum transfer and does not follow from a statistical mechanics derivation). The total density is denoted by ρ and the partial densities by $\rho_i=x_i\rho$ (the number fractions x_i are such that $\Sigma_i x_i=1$). The temperature of species i is T_i, defined from the mean kinetic energy of subpopulation i: $T_i=\langle m_iv_i^2\rangle/d$. Only for an elastic system is the energy equipartition $T_i=T,\forall i$ recovered [6,13–23]. It is found in Appendix B that the pressure in dimension d reads

$$P=\sum_i\rho_iT_i+\rho\eta 2^{d-1}\sum_{i,j}x_ix_j\frac{m_j}{m_i+m_j}(1+\alpha_{ij})T_i\frac{\sigma_{ij}^d}{\langle\sigma^d\rangle}\chi_{ij}, \tag{4}$$

independent of α_{ij}^t, where $\sigma_{ij}=(\sigma_i+\sigma_j)/2$, $\langle\sigma^d\rangle=\Sigma_i x_i\sigma_i^d$, η is the packing fraction (e.g. $\eta=\pi\rho\langle\sigma^3\rangle/6$ in three dimensions), and the χ_{ij} are the pair correlation functions at contact. The latter (unknown) quantities may be approximated by their elastic counterparts (see Ref. [24] for a general procedure to infer reliable pair correlation functions in a multicomponent d-dimensional hard-sphere fluid from the equation of state of the monodisperse system). In the following analysis, it will turn sufficient to include only the low-density behavior, $\chi_{ij}=1$, to improve upon the ideal equation of state $P=P^{\text{ideal}}=\Sigma_i\rho_iT_i$, that holds for $\rho\to0$ only. We emphasize that no approximation has been made on the single-particle velocity distribution in the derivation of Eq. (4) (the key assumption is that the two-body distribution function factorizes at contact in a product of the single-particle distribution [25]).

It is instructive to check the validity of our equation of state by considering the elastic limit where $\alpha_{ij}=1$ and $T_i=T$. A straightforward calculation (under the reasonable and often made assumption that $\chi_{ij}=\chi_{ji}$) shows that the mass ratio simplifies and expression (4) may be cast in the form

$$\frac{P}{\rho T}=1+\eta 2^{d-1}\sum_{i,j}x_ix_j\frac{\sigma_{ij}^d}{\langle\sigma^d\rangle}\chi_{ij}, \tag{5}$$

which is the correct result (see, e.g., Ref. [26]). In particular, for the single-species (monodisperse) problem, we recover the virial relation $P/(\rho T)=1+2^{d-1}\eta\chi$. Note that Eq. (5) corresponds to the equation of state put forward in Ref. [27], which thus neglects the inelasticity of the collisions and the associated breakdown of kinetic energy equipartition. On the other hand, our approach fully incorporates these two features.

We finally generalize Eq. (4) to the situation of a continuous size distribution, with a probability density distribution $W(\sigma)$ (normalized to 1 so that $\langle\sigma^n\rangle=\int\sigma^nW$); the temperature is, in general, a continuous function $T(\sigma)$ of size and

$$\frac{P}{\rho}=\int W(\sigma)T(\sigma)d\sigma+\frac{\eta}{2}\int d\sigma d\sigma' W(\sigma)W(\sigma')\frac{m_{\sigma'}}{m_\sigma+m_{\sigma'}}(1+\alpha_{\sigma\sigma'})T(\sigma)\frac{(\sigma+\sigma')^d}{\langle\sigma^d\rangle}\chi_{\sigma\sigma'}. \tag{6}$$

In the following sections, the above equation of state will be used to test hydrodynamic predictions for a monodisperse system and for a binary mixture.

III. MOLECULAR DYNAMICS SIMULATIONS FOR THE ONE-COMPONENT SYSTEM

A. Introduction

We have implemented molecular dynamics simulations with an event-driven algorithm for N spherical particles in a two-dimensional $L\times L$ box. Periodic boundary conditions are enforced in the x direction, while the energy loss due to collisions is compensated by an energy injection by two walls situated at $y=0$ and $y=L$ (we consider the amplitude of motion of the walls to be small so that their positions are considered as fixed [1], which avoids the complication of heat pulses propagating through the system [28]). We will refer to the y direction as the ''vertical'' one, although we are interested in regimes for which gravity can be neglected [7] (i.e., when the shaking is violent enough). The energy can be injected in two ways:

(1) By *thermal walls* that impose a given temperature of order T_0 [29]. When a particle collides with the wall, its new vertical (along y) velocity is extracted at random from the

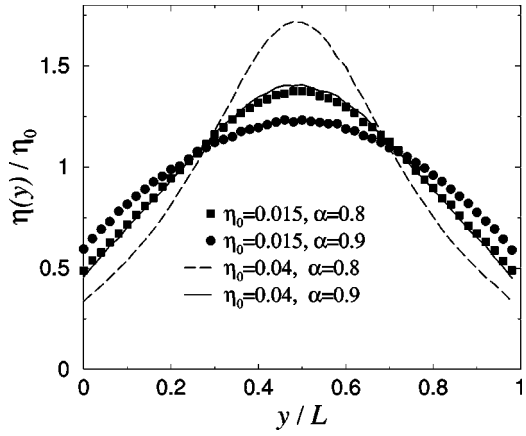

FIG. 1. Density profiles for two normal inelasticities and two densities. In all cases, the number of particles is $N=500$. The symbols correspond to the smallest density (the mean packing fraction averaged over the whole system is $\eta_0=0.015$) and the lines are for a higher density ($\eta_0=0.04$). The ratio $\eta(y)/\eta_0$ is also the ratio $\rho(y)/\rho_0$ of local density normalized by the mean one.

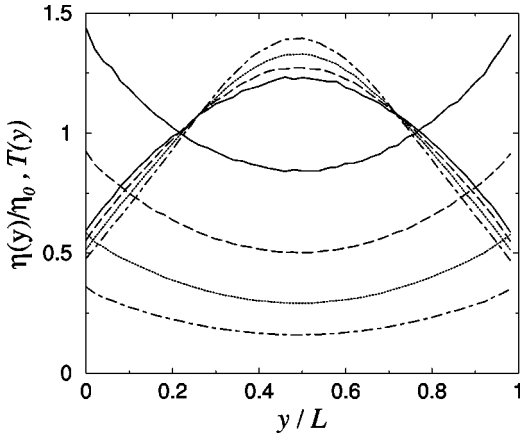

FIG. 2. Density profiles $\eta(y)/\eta_0$ (upward curves) and temperature profiles (downward curves) for a given normal restitution coefficient $\alpha=0.9$ and different tangential restitutions ($N=500$ particles, mean packing fraction $\eta_0=0.015$). The temperature is the total one (including horizontal and vertical degrees of freedom); it is expressed in arbitrary units but all curves correspond to the same velocity of the vibrating piston. From top to bottom for the temperature $T(y)$ and from bottom to top for the density, the curves correspond, respectively, to $\alpha^t=-1$, $\alpha^t=-0.8$, $\alpha^t=-0.5$, and $\alpha^t=0.2$.

probability distribution function $v/\sqrt{T_0}\exp[-v^2/(2\sqrt{T_0})]$, whereas v_x is unaffected.

(2) By *vibrating walls*. For simplicity, we consider walls of infinite mass moving in a sawtooth manner; all particles colliding with a wall find it with the same velocity $v_0>0$ at $y=0$, $-v_0$ at $y=L$. The particle-wall collisions are considered elastic. A particle of velocity $\boldsymbol{v}$ with $v_y<0$ colliding with the bottom wall at $y=0$ (respectively, $v_y>0$ at the upper wall) experiences its velocity change to $\boldsymbol{v}'$ according to $v_y'=2v_0-v_y$ (respectively, $v_y'=-2v_0-v_y$), whereas the x component is unaffected ($v_x'=v_x$).

In both cases, energy is injected in the vertical direction only, and transferred to the other degrees of freedom through interparticle collisions. The vibrating walls being the situation closer to the experimental one, most of our results will be presented in this case, and the effect of injection modes will be briefly discussed.

In this section, we consider the monodisperse case. All particles have the same mass $m(=1)$, diameter σ, and restitution coefficients α and α^t. Most of the simulations are done with $N=500$ particles, and some with $N=1000$ particles (low enough to avoid clustering or inelastic collapse). For our two-dimensional system, the local packing fraction at height y, where the local density is $\rho(y)$, is defined as $\eta(y)=\pi\rho(y)\sigma^2/4$. The global (mean) packing fraction is denoted η_0; $\eta_0=\int_0^L\eta(y)dy/L$.

Starting from a random configuration of the particles (with the constraint of no overlap), we let the system evolve until a steady state is reached. Data on density and temperature profiles as well as on velocity distributions are monitored as time averages; the various quantities are averaged along the x direction since the system remains homogeneous in this direction.

B. Density and temperature profiles

The first observations concern the density and temperature profiles: Figures 1 and 2 show that the density is lower near the walls, where the temperature is higher as expected since energy is injected at the walls and dissipated in the bulk of the system [30]. The profiles are qualitatively similar for thermal or vibrating boundaries. Moreover, the whole temperature profile is proportional to the temperature T_0 imposed by a thermal wall or to the square of the velocity v_0 of the vibrating boundary, while a change in T_0 or v_0 does not change the density profile (not shown). As the mean density increases or α decreases, the profiles get more heterogeneous; as α^t is increased, more energy is transferred to rotational degrees of freedom, so that the temperature decreases, while the density profiles become slightly more peaked (Fig. 2).

Figure 3 clearly shows another feature resulting from the energy injection into the vertical direction: the temperature is anisotropic, i.e., $\langle v_x^2\rangle\neq\langle v_y^2\rangle$, with $T_y>T>T_x$. The anisotropy $A(y)=(T_y-T_x)/(2T)$ is larger at the boundaries, where energy is fed into the vertical direction, decreases due to interparticle collisions, and reaches a plateau in the middle of the slab. The plateau value decreases for increasing number of particles or increasing densities (not shown), as in experiments [8]; the global anisotropy profile and the plateau values are comparable to experimental values [8].

C. Equation of state and hydrodynamics

The equation of state derived in Sec. II reduces, in the case of a two dimensional one-component homogeneous system, to the relation

$$P=\rho T[1+(1+\alpha)\eta\chi], \tag{7}$$

where χ, the pair correlation function at contact, depends on

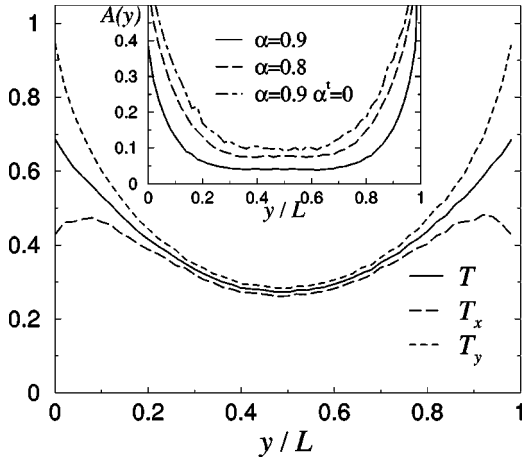

FIG. 3. Temperature profile for $\alpha=0.9$ and $\eta_0=4\%$. The horizontal temperature T_x, vertical temprature T_y, and the total temperature $T=(T_x+T_y)/2$ are shown. The inset shows the anisotropy factor $A=(T_y-T_x)/(2T)$ as a function of height.

the packing fraction η. We will use the form $\chi=(1-7\eta/16)/(1-\eta)^2$, which has been shown to be accurate for elastic hard-disk liquids [31].

The hydrodynamic equations (see Appendix C and Ref. [1]) lead to $\partial_y P=0$ in the absence of a flow field. We check in Fig. 4(a) the constancy of P with y by plotting the ideal gas contribution $\rho(y)T(y)$ (lines) and $P(y)$ given by Eq. (7) (i.e., ideal gas contribution plus Enskog correction). While, at small enough densities (not shown), $\rho(y)T(y)$ is constant in the bulk ($y\in[0.2L,0.8L]$), the Enskog correction is necessary for the densities used in Fig. 4 (note that the density can be quite larger in the middle of the system than at the boundaries). We also note that the inelasticity term $(1+\alpha)$ is relevant, although small at the densities presented [the profiles of $\rho T(1+2\eta\chi)$, not shown, display a less uniform shape with y, the effect being stronger at larger densities]. In all cases, boundary layers ($y<0.2L$ and $y>0.8L$) are observed [1] in which the pressure decreases. This discrepancy can be related to the anisotropy described in the preceding section (pressure and temperature are most anisotropic near the walls).

The comparison with hydrodynamics may be improved as follows. The pressure tensor $\boldsymbol{P}$ is diagonal in the present no-flow situation, but has different xx and yy components, and the homogeneity along the x direction implies that the condition of vanishing flow field $\boldsymbol{\nabla}\cdot\boldsymbol{P}=0$ reduces to $\partial_y P_{yy}=0$. We therefore check in Fig. 4(b) that the y-y component of the pressure tensor, given by the equation of state (7) with the total temperature $T=(T_x+T_y)/2$ replaced by its vertical component T_y, is uniform in the whole system. With Enskog correction, the corresponding profiles are remarkably flat. This result could be tested in experimental situations in which both T_x and T_y are measured. Such an analysis validates both the hydrodynamic picture and the equation of state proposed by automatically sampling several densities in a single run.

At low densities, assuming the ideal gas equation of state to hold, the hydrodynamic study of Ref. [1] (recalled in Appendix C), leads to the following analytical prediction for the temperature profile:

$$\frac{y}{L}=\frac{\xi+\sinh\xi\cosh(\xi_m-\xi)}{\xi_m+\sinh\xi_m},$$

$$\xi=\frac{\xi_m}{2}\pm\cosh^{-1}\left(\sqrt{\frac{T}{T_0}}\cosh\frac{\xi_m}{2}\right), \tag{8}$$

where T_0 is the temperature at the boundaries and ξ_m is proportional to the total number of particles. The corresponding fits of the temperature profiles are shown in Fig. 5; a good agreement is obtained, especially at lower densities as expected [since the ideal gas equation of state is a crucial ingredient in the derivation of Eq. (8)]. We use one fitting parameter ξ_m to obtain T/T_0 [32]. Figure 4 showed that consideration of the "vertical" pressure P_{yy} led to a better agreement with hydrodynamic predictions than the total $P_{xx}+P_{yy}$. A similar conclusion is incorrect for the temperature profiles: the transport equation for the temperature is scalar [see Eq. (C2)], and Eq. (8) holds for the total T, not for the vertical T_y.

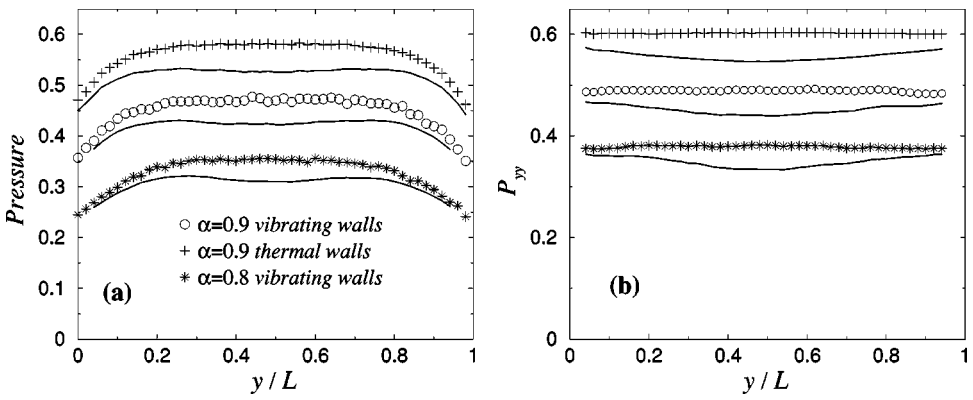

FIG. 4. Pressure given by the equation of state (7). (a) The symbols correspond to $P=\rho(y)T(y)[1+(1+\alpha)\eta(y)\chi(y)]$ (see text), where T is the total temperature. The lines immediately below a given set of symbols show the ideal gas contribution $\rho(y)T(y)$ only. For the three situations investigated, the mean density is the same ($\eta_0=0.04$). (b) Same figure with the vertical temperature T_y instead of T inserted in the equation of state, yielding therefore the yy component of the pressure tensor.

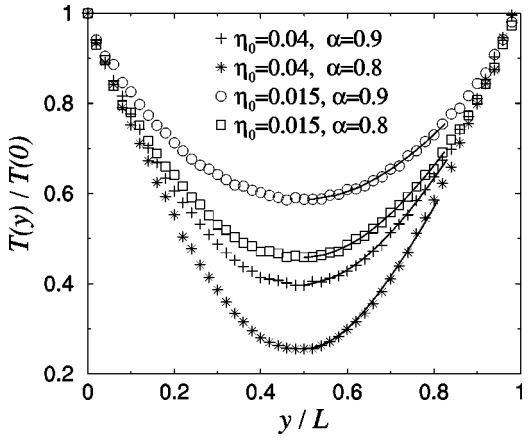

FIG. 5. Fits of the temperature profiles measured in MD with the analytical expression (8). The fits are shown with continuous curves while the symbols stand for the MD measures. For clarity, the fits are restricted to heights $L/2 \leqslant y \leqslant 0.8L$.

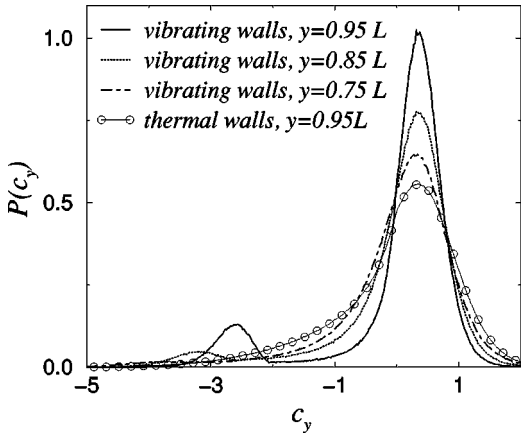

FIG. 6. Probability distribution function of the vertical velocity component $c_y = v_y/\sqrt{T_y}$ for different heights. By definition, $\langle c_y^2 \rangle = 1$, whatever the altitude y. Here, $\eta_0 = 0.04$, $N = 500$, $\alpha = 0.9$, and $\alpha^t = 0$.

D. Velocity distributions

Because of the energy injection through the walls, the velocity distributions are anisotropic, and *a priori* depend on the distance to the walls. The vertical velocity distribution also depends on the nature of the walls as shown in Fig. 6. A smooth distribution is obtained in the vicinity of a thermal wall, while the incoming and outcoming particles yield two separated peaks for vibrating walls (see also Ref. [1]).

On the other hand, the *rescaled* horizontal velocity distribution $P(c_x)$ (with $c_x = v_x/\sqrt{T_x}$) is remarkably independent of the distance from the walls (outside the boundary layers), even if the temperature changes with y, at small enough densities (this result was also obtained in Ref. [29]). At larger densities, $P(c_x)$ becomes slightly dependent on y, as also seen in recent similar MD simulations [33]. Figure 7 shows clearly non-Gaussian features similar to the experimentally observed ones [7,13,34], with in particular overpopulated both small-velocity and high-velocity regions. A slight dependence on the parameters is obtained: $P(c_x)$ broadens if the inelasticity increases (i.e., if α decreases), if α^t increases, or if η_0 or N increase. Experimentally, the dependence on density or material properties is weak and difficult to measure [7] but seems to exist, in particular as far as N is varied [9]. The angular velocity distributions, also displayed in Fig. 7, share a similar non-Gaussian character and the same dependence with the parameters.

As density or inelasticity are further increased, clustering phenomena may occur, leading to heterogeneities along the x direction, with the coexistence of colder, denser regions with hotter, less dense ones. The average over the x direction then leads to artificially broad $P(c_x)$.

Finally, as a general rule, thermal walls lead to slightly broader velocity distributions than vibrating walls.

E. Effective restitution coefficients

We now turn to the study of the effective inelasticities introduced in the context of a random restitution coefficient (RRC) model [10,11]: even if the restitution coefficient α is constant, the energy is injected in the vertical direction and transferred to other degrees of freedom through collisions, so that the *effective* restitution coefficient for collisions projected onto the x direction,

$$\alpha_{1d} = \frac{v'_{12,x}}{v_{12,x}}, \tag{9}$$

may be either smaller or larger than 1 (see Ref. [3] for a related discussion).

Values of α_{1d} have been experimentally measured [9,11]

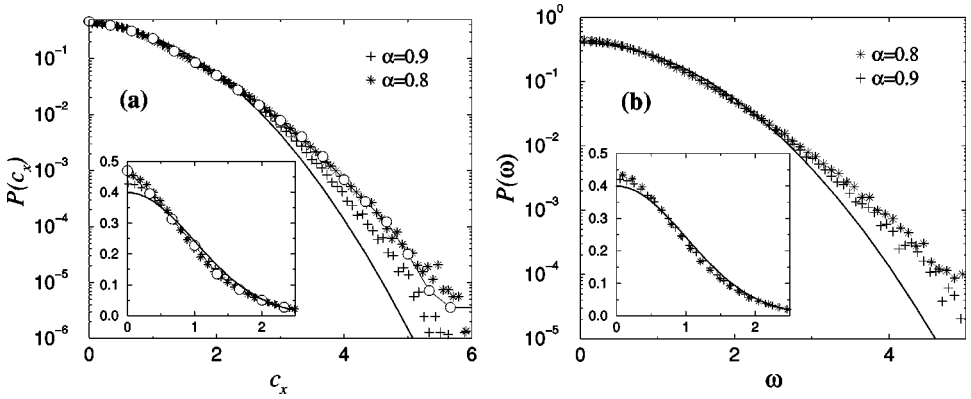

FIG. 7. (a) Probability distribution function of the rescaled horizontal velocity component $c_x = v_x/\sqrt{T_x}$, on a linear-log plot. Here $\eta_0 = 0.015$, $N = 500$, $\alpha = 0.9$ (pluses), 0.8 (stars), and $\alpha^t = 0$. The solid line is the Gaussian with unit variance, the circles correspond to experimental data [7,9] for steel beads. (b) Probability distribution function of the angular velocities for the same parameters.

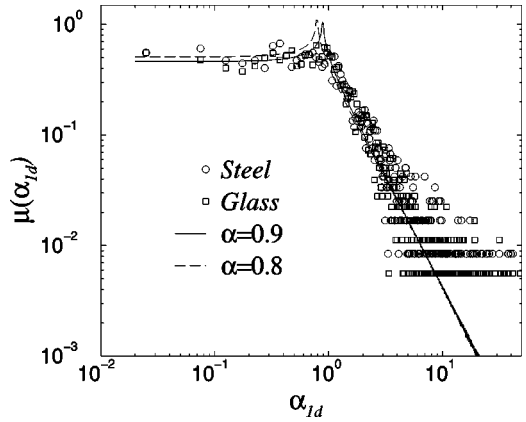

FIG. 8. Probability distribution function of effective one-dimensional restitution coefficients α_{1d}. The MD results are compared to the experimental measures of Feitosa and Menon [9] on steel and glass samples (for which the nominal restitution coefficient may be considered close to 0.9).

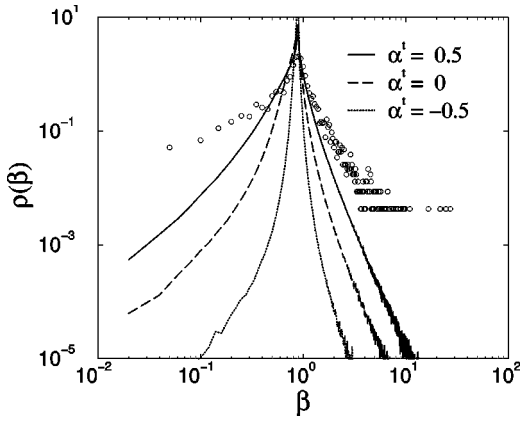

FIG. 10. Probability distribution function of energy restitution coefficients β. Various tangential restitution coefficients α^t are considered for $\alpha=0.9$ and $\eta_0=1.5\%$. The circles represent the experimental data for steel grains [9].

and shown to display a broad probability distribution $\mu(\alpha_{1d})$ very similar for various materials and densities. We have measured α_{1d} for many collisions and thus obtained its distribution, displayed in Fig. 8 together with experimental data for steel and glass beads. A remarkable agreement is found [35], with a broad range of possible values for α_{1d}. Our study shows, in particular, that $\mu(\alpha_{1d})$ displays a α_{1d}^{-2} tail for $\alpha_{1d}>1$, irrespective of α, α^t, and density.

The importance of the correlations between α_{1d} and the relative velocity $\boldsymbol{g}=\boldsymbol{v}_{12}/\sqrt{2T}$ of the colliding particles has been emphasized in Ref. [11] and is revealed by the computation of $\mu(\alpha_{1d}|g_x)$, the distribution of α_{1d} being conditioned by a given value of g_x; although no precise experimental determination of the conditional $\mu(\alpha_{1d}|g_x)$ could be achieved in Ref. [11], strong evidences for a sharp cutoff $\propto 1/g_x$ at large values of α_{1d} were provided and the form $\mu(\alpha_{1d}|g_x)\propto\exp[-(\alpha_{1d}g_x)^2/R]$ at large α_{1d} has been proposed. The conditional $\mu(\alpha_{1d}|g_x)$ obtained in the present MD simulations confirm the above picture; they are displayed in Fig. 9 and show an $\exp[-(\alpha_{1d}g_x)^2/R]$ decrease for the case of vibrating walls (closer to the experimental situation), and a broader form $\exp[-(\alpha_{1d}g_x)/R']$ for thermal walls. Moreover, although $\mu(\alpha_{1d})$ is not sensitive to the various parameters, the cutoff R increases [i.e., leads to broader $\mu(\alpha_{1d}|g_x)$] if α decreases, and if α^t or η_0 increases.

Finally, the *energy* restitution coefficient

$$\beta=\frac{|\boldsymbol{v}'_{12}|}{|\boldsymbol{v}_{12}|} \tag{10}$$

may also be viewed as a random variable that can take values larger than unity due to energy transfers between rotational and translational degrees of freedom [9,11]. Figure 10 displays the probability distribution function (PDF) $\rho(\beta)$ obtained in the MD simulations for various values of α^t, together with the experimental data of Refs. [9,11] for steel beads. $\rho(\beta)$ becomes wider as α^t is increased, but the experimental distribution is broader, which may be traced back to the fact that in the experiments mentioned above, the beads can rotate in three dimensions, whereas our simulations are limited to 2D rotations.

The evolution with the parameters of the distributions μ, ρ, and of the velocity PDF $P(c_x)$ are clearly linked in our simulations: broader conditional $\mu(\alpha_{1d}|g_x)$ corresponds to broader velocity distributions; for instance, both broader μ and $P(c_x)$ are obtained if α decreases, or, at fixed parameters, if vibrating walls are replaced by thermal walls. This connection is in agreement with the phenomenology put forward in the context of the effective RRC model [10,11]. In the RRC approach, the d-dimensional system with energy injection along a preferential direction is replaced by a

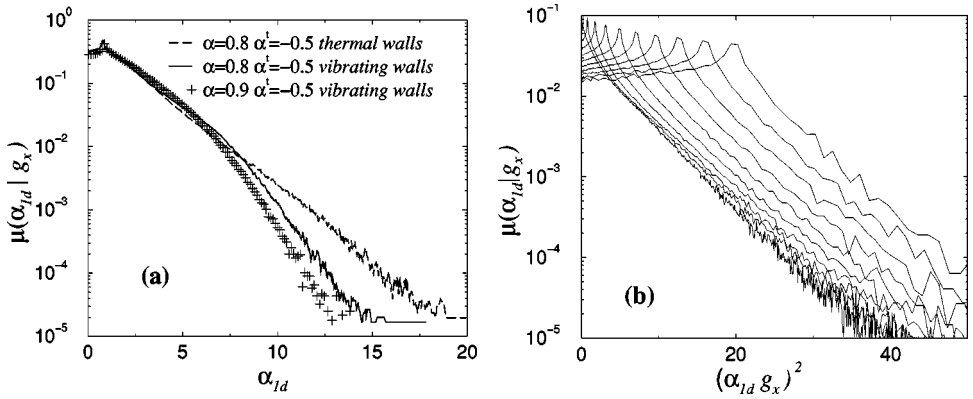

FIG. 9. (a) Conditional PDF of α_{1d} for a given value g_x of order unity. Note the different shapes for thermal and vibrating walls. (b) Same, but as a function of $(\alpha_{1d}g_x)^2$ (and $g_x=0.2,0.5,1.0,1.5,2.0,3.0,4.0,5.0$) for vibrated walls with $\alpha=0.9$, $\alpha^t=0$, and $\eta_0=0.015$.

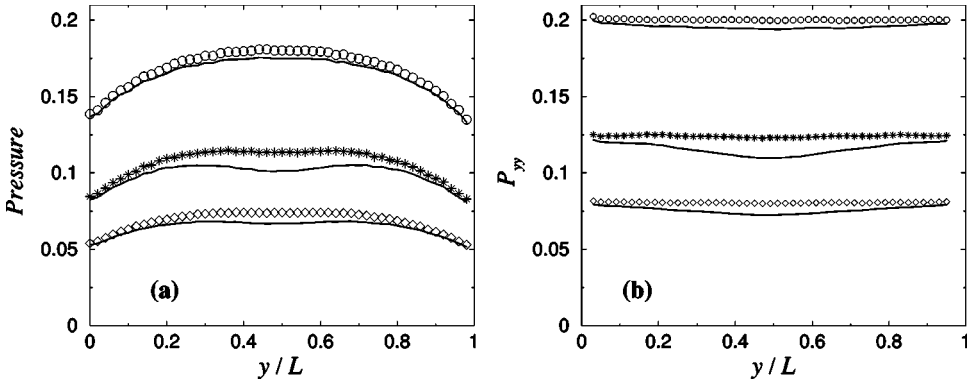

FIG. 11. (a) The symbols show the pressure calculated from the complete equation of state for a binary mixture (11) including Enskog correction, while the lines immediately below display the ideal gas contribution $\rho_1(y)T_1(y)+\rho_2(y)T_2(y)$ to the pressure. The three sets of curves correspond to: *upper set*, $\eta_0=0.015$, $\alpha_{11}=0.9$, $\alpha_{12}=0.8$, $\alpha_{22}=0.7$, $m_1=5m_2$; *middle set*, $\eta_0=0.04$, $\alpha_{11}=0.9$, $\alpha_{12}=0.8$, $\alpha_{22}=0.7$, $m_1=3m_2$; *lower set*, $\eta_0=0.04$, $\alpha_{11}=0.7$, $\alpha_{12}=0.8$, $\alpha_{22}=0.9$, $m_1=3m_2$. (b) Same curves, where the temperatures are the vertical ones ($T_{i,y}$) instead of the total $T_i=(T_{i,x}+T_{i,y})/2$, yielding therefore the yy component of the pressure tensor.

$(d-1)$-dimensional projected *effective* system in which the restitution coefficient is a random variable [10] correlated with the relative velocities of the colliding particles [11]. In the present situation, $d=2$ and the effective model is one dimensional. Although the real projected collisions are not stochastic, one effectively injects at each collision a restitution coefficient randomly chosen from the distribution $\mu(\alpha_{1d}|g_x)$. Taking μ as an input for the model, close to the experimental data, one obtains velocity distributions as output, in good agreement with the experimental ones. The link between μ and $P(c_x)$ can be studied [11], and broader conditional distributions $\mu(\alpha_{1d}|g_x)$ yield broader $P(c_x)$ (at large c_x, compared to the Gaussian), as in our more realistic simulations.

IV. MOLECULAR DYNAMICS SIMULATIONS FOR THE BINARY MIXTURE

In this section, we investigate the properties of vibrated binary mixtures; such systems have recently attracted much attention, both on the experimental [6,13,14] and theoretical sides [15–23,36,37]. In particular, the breakdown of energy equipartition between the two constituents of the mixture has been thoroughly investigated.

The main difference with previous studies consists here in the realistic character of both MD simulations (as opposed to Monte Carlo methods) and the energy injection mechanism at the boundaries; the setup is the same as in the preceding section, with, however, two types of particles, with masses m_1, m_2, and sizes σ_1, σ_2. The three normal restitution coefficients (corresponding to the three possible types of collisions) are α_{11}, $\alpha_{12}=\alpha_{21}$, α_{22}. In the context of a forcing mechanism through a random external force [25,38], it has been shown that the influence of size ratio on the temperature ratio measuring the energy nonequipartition was rather weak [17] compared to that of inelasticity parameters or mass ratio. We shall consequently limit our study to identical sizes $\sigma_1=\sigma_2$ in two dimensions, which corresponds to the experimental situation we will refer to [6,9]. For simplicity, the tangential restitution coefficients α_{ij}^t are also taken equal.

As in the monodisperse case, we measure density and temperature profiles, velocity distributions, as well as the temperature ratios $\gamma(y)=T_2(y)/T_1(y)$, $\gamma_x(y)=T_{2,x}(y)/T_{1,x}(y)$, $\gamma_y(y)=T_{2,y}(y)/T_{1,y}(y)$. Some comparison with experimental data [6,9] will be proposed whenever possible.

A. Equation of state

We first test the equation of state (4) in Fig. 11. As in the monodisperse case, the Enskog correction is clearly relevant, even at low global densities, since the density profiles reach relatively high values for $y\simeq L/2$. It is, however, sufficient to truncate the equation of state at second virial order, which amounts to taking the low-density limiting value $\chi_{ij}=1$ for the pair correlation functions at contact:

$$P\simeq\rho_1T_1+\rho_2T_2+\frac{\pi\sigma^2}{2(m_1+m_2)}[(1+\alpha_{11})\rho_1^2m_2T_1 + (1+\alpha_{12})\rho_1\rho_2(m_1T_2+m_2T_1)+(1+\alpha_{22})\rho_2^2m_1T_2]. \tag{11}$$

Moreover, the boundary layer in which the anisotropy is strong is still apparent if the global temperatures T_1 and T_2 are used, while use of the vertical ones ($T_{1,y}$ and $T_{2,y}$), suggested by the anisotropy of temperatures and pressure as in the monodisperse case, leads to a uniform yy component of the pressure tensor in the whole system. The functional dependence of pressure upon densities is therefore accurately reproduced by the equation of state (11).

Although we have not extended the hydrodynamic approach of Brey *et al.* [1] to binary mixtures (it would be possible making use of the Navier-Stokes-like equations derived in Ref. [36] where only the overall temperature associated with both species serves as a hydrodynamic field, but where the transport coefficients explicitly depend on temperature ratio), we see in Fig. 12 that the temperature profiles can be fitted, at low density, by the form (8). We emphasize that there is no fundamental reason for the agreement. The quality of the fit is much better for the less massive particles

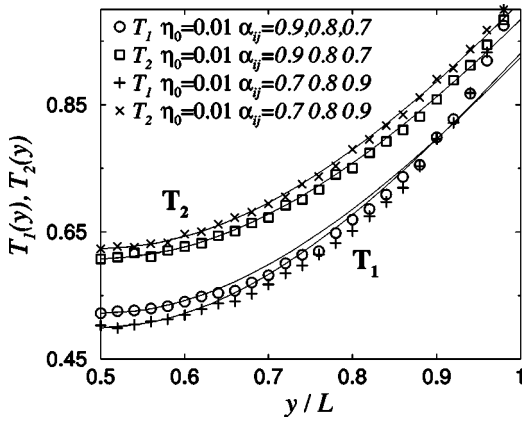

FIG. 12. Temperature profiles for an equimolar granular mixture, driven by vibrating walls. The symbols show the MD measures, and the lines are fits to the analytical expression derived for the single-component case. In all cases, the particle 1 (the heaviest) has mass $m_1=3m_2$; its temperature T_1 corresponds to the two lower sets.

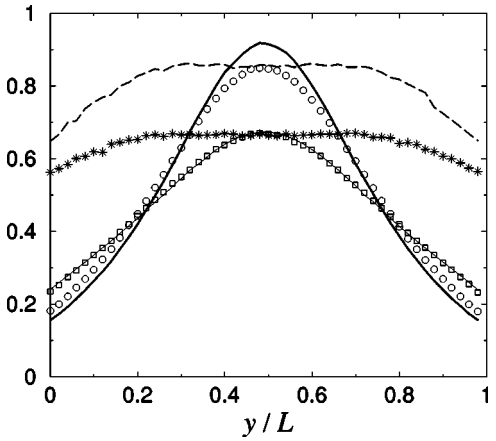

FIG. 14. Density profiles and temperature ratio profiles (binary mixture, vibrating walls). The lines correspond to $\alpha_{ij}=0.7;0.8;0.9$, whereas the symbols are associated with ''reverse'' inelasticities $\alpha_{ij}=0.9;0.8;0.7$. The other parameters are $\alpha^t=0$, $m_1=3m_2$, $\eta_{1,0}=\eta_{2,0}$, and $\eta_0=2\eta_{1,0}=0.015$. The upper flatter curves (dashed line and stars) show the temperature ratio. As in Fig. 13, the density of heavy particles ρ_1 (thick continuous curve and circles) is more peaked and denser in the middle of the cell than that of light grains (thin continuous curve and squares).

whose density is more homogeneous across the system (see the following). For simplicity, we have used the shorthand notation $\alpha_{ij}=0.7;0.8;0.9$ for the situation where $\alpha_{11}=0.7$, $\alpha_{12}=0.8$, and $\alpha_{22}=0.9$.

B. Nonequipartition of translational kinetic energy

The density and temperature profiles are displayed for various values of the parameters in Figs. 13 and 14. The more massive particles (labeled 1), which display a more heterogeneous profile and are denser in the middle of the cell, have typically larger kinetic energies than the lighter ones; generically, $\gamma=T_2/T_1$ is smaller than 1, as in homogeneous mixtures [16,17]. The study of the y dependence of γ shows that γ increases from the boundaries to the center of the system, and is constant across a wide range of y even if T_1 and T_2 vary significantly. As also experimentally shown in Ref. [6], γ is very close to 1 if $m_1=m_2$, even if the inelasticities of the particles are different. It decreases if the mass ratio increases (Fig. 13), but displays only a very weak (but strikingly similar to experimental data) sensitivity on the global density (Fig. 15) as well as on the relative densities of heavy and light particles; moreover, γ may increase or decrease as $\eta_{1,0}/\eta_{2,0}$ is increased (see Fig. 16), depending on the relative inelasticities.

The anisotropy in the temperatures yield an anisotropic γ; we obtain, $\gamma_x>\gamma>\gamma_y$, as in experiments [9], also with different shapes. γ_x decreases from the walls to the center while γ and γ_y increase (Fig. 15). All these results are in very good agreement with the existing experimental results for two-dimensional vibrated mixtures [6,9]. We summarize in Tables I and II some of the effects reported here.

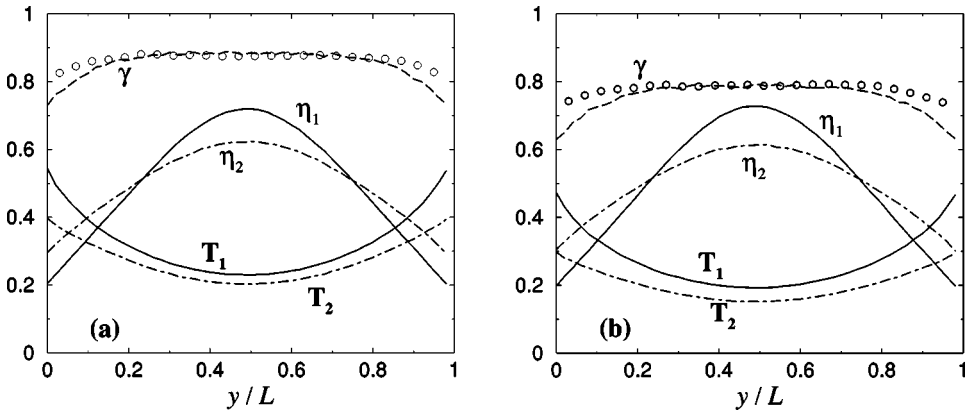

FIG. 13. (a) Vertical profiles for a binary mixture with $m_1=3m_2$, $\eta_0=0.015$, $\alpha_{ij}=0.85$, $N=500$, and equal mean densities $\eta_{1,0}=\eta_{2,0}$ (excitation by vibrating walls). From bottom to top: temperature profiles of both species, density profiles $\eta_2(y)/(2\eta_0)$ and $\eta_1(y)/(2\eta_0)$. Since $\sigma_1=\sigma_2$, the packing fraction η_i is proportional to the local density ρ_i of species i. The upper dashed curve shows the temperature ratio $\gamma=T_2/T_1$ as a function of height, and the circles show the same quantity for a nonequimolar mixture where $\eta_{1,0}=8\eta_{2,0}$. (b) Same with a higher mass ratio $m_1=5m_2$.

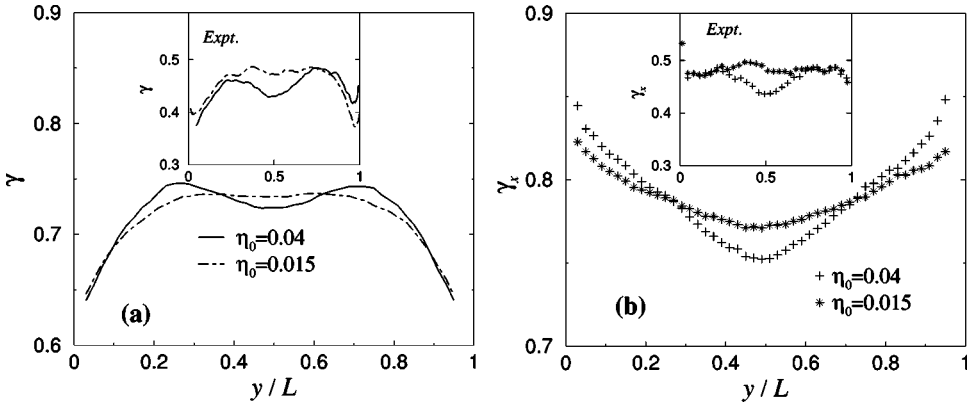

FIG. 15. Effect of density on the temperature ratio for $m_1=3m_2$, $\alpha_{ij}=0.9;0.8;0.7$ (vibrating walls). (a) shows the total ratio T_2/T_1 and (b) shows the ratio of horizontal temperatures $T_{2,x}/T_{1,x}$. In both cases, the corresponding experimental measures are shown in the insets for a steel-glass mixture (at different densities, but with a density ratio of 2, close to that of the MD simulations 0.04/0.015≃2.6). The purpose is to show that the changes induced by density in MD are qualitatively the same as in the experiments.

When rotations are included (and thus $\alpha^t>-1$), γ decreases. Moreover, the ratio of rotational kinetic energies γ_r can then be measured. As shown in Tables I and II, γ_r takes values of the same order as γ. This quantity may also be computed from experimental data, although measures of rotational velocities are *a priori* more difficult than that of translational ones.

The measured values of γ are of the same order as the experimental data. We do not however try to obtain a precise numerical agreement for the following reasons:

(i) In the experiments of Ref. [6], the beads can rotate in three dimensions, whereas the simulated spheres rotate in two dimensions only. Since α^t has a strong effect on γ, we suspect that this difference between experiments and simulations may affect γ. Moreover, the experimental value of α^t is not known, and the precise validity of the inelastic hard-sphere model with a tangential restitution coefficient should be assessed

(ii) Different energy injection mechanisms (thermal vs vibrating walls, homogeneous driving vs injection at the boundaries) lead to different values of γ. Even if the energy injection by vibrating walls is reasonably realistic, such a sensitivity of γ renders its precise numerical prediction elusive.

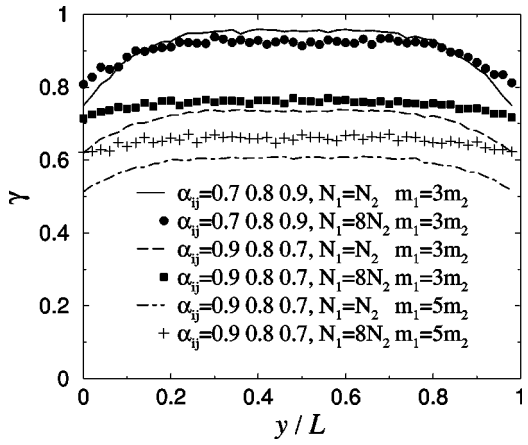

FIG. 16. Influence of number fraction on the temperature ratio T_2/T_1. The total number of particles is $N=N_1+N_2=500$ (vibrating walls). Given that $\sigma_1=\sigma_2$, $N_1/N_2=8$ corresponds to $\eta_{1,0}=8\,\eta_{2,0}$.

Nonetheless, the *qualitative* very good agreement, even for subtle effects (see, e.g., Fig. 15), between numerics and experiment, and the possibility to change the various parameters in the simulations allow us to make some predictions on the effect of various parameters. For example, increasing the mass ratio should yield smaller values of γ (Fig. 13). Moreover, Fig. 14 makes it clear that the value of γ, at given mass ratio, is smaller for inelasticities $\alpha_{ij}=0.9;0.8;0.7$ than with ''reverse'' inelasticities $\alpha_{ij}=0.7;0.8;0.9$. This effect was already noted in Ref. [17] and has the following intuitive interpretation: when the more massive particles are more inelastic, they lose more energy, their temperature decreases, which results in a higher γ. We therefore predict that in the context of the experiments reported in Ref. [6], a mixture of steel and aluminum ($\alpha_{steel}\approx 0.9, \alpha_{al}\approx 0.83, m_{steel}\approx 3m_{al}$) should yield a smaller value of γ than the brass-glass mixture ($\alpha_{brass}\approx 0.8, \alpha_{glass}\approx 0.9, m_{brass}\approx 3m_{glass}$) for which the measured γ is close to 0.6–0.7. The dependence of γ upon number fraction $x_i=\rho_i/\rho$ may, on the other hand, be counterintuitive: at a given mean density ρ_0, an increase of the relative fraction x_1 of heavy particles leads to an increase of γ when the heavy particles are the more elastic (see Fig. 16).

TABLE I. Values of γ, γ_x, γ_r in the middle of the system for $N=500$, $\alpha_{ij}=0.85$, $\eta_{1,0}=\eta_{2,0}$, $m_1=3m_2$ (first three lines), and $m_1=5m_2$ (last three lines).

α^t	γ	γ_x	γ_r
−1	0.88	0.92	
−0.5	0.825	0.89	0.83
0	0.79	0.86	0.8
−1	0.79	0.845	
−0.5	0.7	0.78	0.69
0	0.65	0.74	0.66

TABLE II. Values of γ, γ_x, γ_r in the middle of the system for $N=500$, $\alpha_{ij}=0.9,0.8,0.7$ (first three lines), and $\alpha_{ij}=0.7,0.8,0.9$ (last three lines), $m_1=3m_2$, $\eta_{1,0}=\eta_{2,0}$.

α^t	γ	γ_x	γ_r
−1	0.735	0.775	
−0.5	0.69	0.735	0.735
0	0.665	0.72	0.72
−1	0.95	1.0	
−0.5	0.89	0.99	0.84
0	0.85	0.96	0.81

This effect was also clearly observed for the homogeneously heated mixture [17]. On the other hand, an increase of x_1 leads to a relatively weak decrease of γ when the heavier particles are the less elastic, whereas the opposite (albeit also quite weak) trend could be observed in Ref. [17].

C. Velocity distributions

As in the monodisperse case, we have measured the single-particle velocity distributions, which are anisotropic as expected. The vertical velocity distributions are similar to those shown in Fig. 6, and the horizontal velocity distributions show strong non-Gaussian features, as in the monodisperse case. Moreover, it appears in Fig. 17 that the rescaled velocity distributions $P_1(c_x)$ and $P_2(c_x)$ are very close (even if not equal, see also Ref. [23]) for both types of particles. The differences between $P_1(c_x)$ and $P_2(c_x)$ increase if the inelasticities or the mass ratio increase. $P_i(c_x)$ depend slightly on the various parameters, in the same way as the velocity distributions of the monodisperse situation; this dependence would probably be very difficult to measure in an experiment, which would probably lead to the conclusion that $P_1(c_x)\approx P_2(c_x)$.

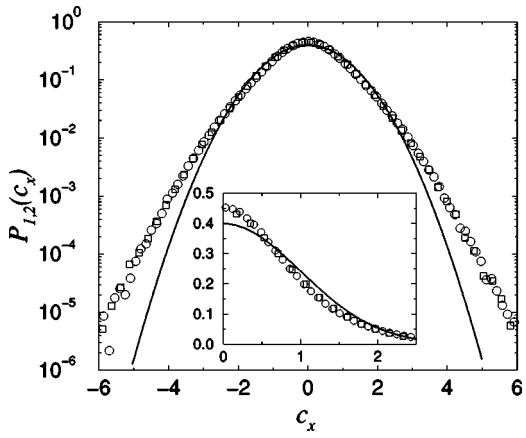

FIG. 17. Probability distribution functions of the rescaled horizontal velocity components $c_{i,x}=v_{i,x}/\sqrt{T_{i,x}}$, for an equimolar mixture. Squares are for P_1 (heavy grains) and circles for P_2 (light grains). Here $\eta_0=0.015$, $N=500$, $\alpha_{ij}=0.9,0.8,0.7$, $m_1=3m_2$, and $\alpha^t=0$. The solid line is the Gaussian with variance 1.

V. CONCLUSION

In this study, we have considered vibrated granular gases outside the Boltzmann limit of (very) low densities. The molecular dynamics simulations performed are free of the approximations underlying the usual kinetic theory or hydrodynamic approaches. Taking due account of the first correction to the ideal gas contribution in the equation of state (second virial order), we, however, found a remarkable constant yy component of the pressure tensor over the whole cell, for monodisperse or bidisperse systems, despite the strong density and temperature heterogeneities due to the realistic energy injection mechanism.

The study of the velocity distributions along the horizontal direction (perpendicular to the energy injection) has revealed non-Gaussian features similar to experiments, which depend weakly on the various parameters involved in the model.

The projection of the dynamics onto the horizontal direction has allowed us to gain insight into the correlations between the effective restitution coefficient α_{1d} and the relative velocities g_x of colliding particles. The measured conditional probability distributions $\mu(\alpha_{1d}|g_x)$ are in agreement with the forms proposed in Ref. [11], based upon partial experimental data. The link between $\mu(\alpha_{1d}|g_x)$ and the velocity probability distribution functions [11] has been confirmed.

In the case of binary mixtures we have analyzed the ratio of granular temperatures as a function of the various parameters, and found a very good qualitative agreement with experiments. The velocity distributions of the two components have, moreover, been shown to be very similar.

ACKNOWLEDGMENTS

We would like to thank K. Feitosa and N. Menon for providing us with valuable unpublished data.

APPENDIX A: INCLUSION OF A TANGENTIAL RESTITUTION COEFFICIENT

In this appendix we give the collision rules when a tangential restitution coefficient is introduced (see also Ref. [12]). The two colliding particles labeled (1) and (2) have masses m_i, diameters σ_i, and moment of inertia $I_i=m_i q\sigma_i^2/4$ (with $q=1/2$ for disks and 2/5 for spheres). The precolliding velocities are $\boldsymbol{v}_i,\boldsymbol{\omega}_i$, and postcolliding velocities are denoted with primes.

The normal unit vector is defined as

$$\hat{\boldsymbol{\sigma}}=\frac{\boldsymbol{r}_1-\boldsymbol{r}_2}{|\boldsymbol{r}_1-\boldsymbol{r}_2|}. \tag{A1}$$

The relative velocity of the contact point,

$$\boldsymbol{g}=\boldsymbol{v}_1-\boldsymbol{v}_2-\left(\frac{\sigma_1}{2}\boldsymbol{\omega}_1+\frac{\sigma_2}{2}\boldsymbol{\omega}_2\right)\times\hat{\boldsymbol{\sigma}}, \tag{A2}$$

has normal component $\boldsymbol{g}_n=(\boldsymbol{g}\cdot\hat{\boldsymbol{\sigma}})\hat{\boldsymbol{\sigma}}$ and tangential component $\boldsymbol{g}_t=\boldsymbol{g}-\boldsymbol{g}_n$ (this defines the tangential unit vector $\hat{\boldsymbol{t}}=\boldsymbol{g}_t/|\boldsymbol{g}_t|$.

The postcollisional velocities can be expressed simply in terms of the precollisional velocities through the introduction of the linear momentum change of particle (1),

$$\Delta \boldsymbol{P}=m_1(\boldsymbol{v}_1'-\boldsymbol{v}_1)=-m_2(\boldsymbol{v}_2'-\boldsymbol{v}_2). \tag{A3}$$

Indeed, the change of angular momentum is

$$\frac{2I_i}{\sigma_i}(\boldsymbol{\omega}_i'-\boldsymbol{\omega}_i)=-\hat{\boldsymbol{\sigma}}\times\Delta\boldsymbol{P}. \tag{A4}$$

One obtains

$$\boldsymbol{v}_1'=\boldsymbol{v}_1+\frac{\Delta\boldsymbol{P}}{m_1}, \tag{A5}$$

$$\boldsymbol{v}_2'=\boldsymbol{v}_2-\frac{\Delta\boldsymbol{P}}{m_2}, \tag{A6}$$

$$\boldsymbol{\omega}_i'=\boldsymbol{\omega}_i-\frac{\sigma_i}{2I_i}\hat{\boldsymbol{\sigma}}\times\Delta\boldsymbol{P}. \tag{A7}$$

The normal and tangential components of $\Delta\boldsymbol{P}$ are then computed using the definition of the normal and tangential coefficients of restitution:

$$\boldsymbol{g}_n'=-\alpha\boldsymbol{g}_n, \tag{A8}$$

$$\boldsymbol{g}_t'=-\alpha^t\boldsymbol{g}_t. \tag{A9}$$

Since $\boldsymbol{g}_n=[(\boldsymbol{v}_1-\boldsymbol{v}_2)\cdot\hat{\boldsymbol{\sigma}}]\hat{\boldsymbol{\sigma}}$, the first relation leads to

$$\Delta\boldsymbol{P}\cdot\hat{\boldsymbol{\sigma}}=-\frac{m_1m_2}{m_1+m_2}(1+\alpha)(\boldsymbol{v}_1-\boldsymbol{v}_2)\cdot\hat{\boldsymbol{\sigma}}. \tag{A10}$$

Using the definition of $\boldsymbol{g}_t$, and with $I_i=m_iq\sigma_i^2/4$, one also obtains

$$\boldsymbol{g}_t'=\boldsymbol{g}_t+\Delta\boldsymbol{P}_t\left(\frac{1}{m_1}+\frac{1}{m_2}\right)\left(1+\frac{1}{q}\right), \tag{A11}$$

where $\Delta\boldsymbol{P}_t=(\Delta\boldsymbol{P}\cdot\hat{\boldsymbol{t}})\hat{\boldsymbol{t}}$. Finally,

$$\Delta\boldsymbol{P}=-\frac{m_1m_2}{m_1+m_2}\left((1+\alpha)\boldsymbol{g}_n+\frac{1+\alpha^t}{1+1/q}\boldsymbol{g}_t\right). \tag{A12}$$

APPENDIX B: EQUATION OF STATE FOR A POLYDISPERSE INELASTIC MIXTURE

In this appendix, we adopt a kinetic definition of the total pressure and compute this quantity for an arbitrary homogeneous mixture of species i, with number fraction $x_i=\rho_i/\rho$. Invoking the virial theorem, the excess pressure $P^{\rm ex}=P-P^{\rm ideal}=P-\Sigma_i\rho_iT_i$ is related to the collisional transfer of linear momentum: the partial excess pressure of species i reads (see, e.g., Ref. [39])

$$P_i^{\rm ex}=\lim_{t\to\infty}\frac{1}{dV}\frac{1}{t}\sum_{j,\text{collisional partner of i}}\boldsymbol{r}_{ij}\cdot\delta\boldsymbol{p}_i \tag{B1}$$

$$=\lim_{t\to\infty}\frac{1}{dV}\frac{1}{t}\sum_{j,\text{collisional partner of i}}\frac{m_im_j}{m_i+m_j}(1+\alpha_{ij})\times(\hat{\boldsymbol{\sigma}}\cdot\boldsymbol{v}_{ij})\sigma_{ij}\quad\text{where}\quad\sigma_{ij}=\frac{\sigma_i+\sigma_j}{2}. \tag{B2}$$

In these equations, it is understood that the summation runs over all the collision events involving a particle of type i and an arbitrary partner j, in a large volume of measure V. The collisional transfer appearing in Eq. (B2) is readily computed within Enskog-Boltzmann kinetic theory, where the velocity distribution functions $\varphi_i(\boldsymbol{v})$ obey the set of nonlinear equations,

$$\partial_t\varphi_i(\boldsymbol{v}_1,t)=\sum_{j=1}^{\mathcal{N}_s}\chi_{ij}\sigma_{ij}^{d-1}n_j\int d\boldsymbol{v}_2\int d\hat{\boldsymbol{\sigma}}\Theta(\hat{\boldsymbol{\sigma}}\cdot\boldsymbol{v}_{12})(\hat{\boldsymbol{\sigma}}\cdot\boldsymbol{v}_{12})\left[\frac{1}{\alpha_{ij}^2}\varphi_i(\boldsymbol{v}_1^*)\varphi_j(\boldsymbol{v}_2^*)-\varphi_i(\boldsymbol{v}_1)\varphi_j(\boldsymbol{v}_2)\right], \tag{B3}$$

where Θ denotes the Heaviside distribution and $(\boldsymbol{v}_1^*,\boldsymbol{v}_2^*)$ are the precollisional velocities converted into $(\boldsymbol{v}_1,\boldsymbol{v}_2)$ by the collision rules (1) and (2). Equation (B2) may be rewritten as

$$P_i^{\rm ex}=\frac{1}{2d}\sum_{j=1}^{\mathcal{N}_s}\chi_{ij}\sigma_{ij}^{d-1}n_j\int d\boldsymbol{v}_1d\boldsymbol{v}_2\int d\hat{\boldsymbol{\sigma}}\,\Theta(\hat{\boldsymbol{\sigma}}\cdot\boldsymbol{v}_{12})(\hat{\boldsymbol{\sigma}}\cdot\boldsymbol{v}_{12})\varphi_i(\boldsymbol{v}_1)\varphi_j(\boldsymbol{v}_2)\frac{m_im_j}{m_i+m_j}(1+\alpha_{ij})(\hat{\boldsymbol{\sigma}}\cdot\boldsymbol{v}_{12})\sigma_{ij}. \tag{B4}$$

Summing the contributions of all species, the total excess pressure follows:

$$P^{\rm ex}=\frac{1}{2d}\sum_{i,j}\chi_{ij}\sigma_{ij}^dn_in_j\frac{m_im_j}{m_i+m_j}(1+\alpha_{ij})\int d\boldsymbol{v}_1d\boldsymbol{v}_2\int d\hat{\boldsymbol{\sigma}}\,\Theta(\hat{\boldsymbol{\sigma}}\cdot\boldsymbol{v}_{12})(\hat{\boldsymbol{\sigma}}\cdot\boldsymbol{v}_{12})^2\varphi_i(\boldsymbol{v}_1)\varphi_j(\boldsymbol{v}_2) \tag{B5}$$

$$=\frac{1}{2d}\sum_{i,j}\chi_{ij}\sigma_{ij}^dn_in_j\frac{m_im_j}{m_i+m_j}(1+\alpha_{ij})\left[\int d\hat{\boldsymbol{\sigma}}\,\Theta(\hat{\boldsymbol{\sigma}}\cdot\hat{\boldsymbol{v}}_{12})(\hat{\boldsymbol{\sigma}}\cdot\hat{\boldsymbol{v}}_{12})^2\right]\int d\boldsymbol{v}_1d\boldsymbol{v}_2(v_1^2+v_2^2)\varphi_i(\boldsymbol{v}_1)\varphi_j(\boldsymbol{v}_2), \tag{B6}$$

where $\hat{\boldsymbol{v}}_{12}$ is the unit vector along $\boldsymbol{v}_{12}$, and where the contribution from the dot product $\boldsymbol{v}_1 \cdot \boldsymbol{v}_2$ vanishes by symmetry in the last integral. The integral over the solid angle $\hat{\boldsymbol{\sigma}}$ is related to the volume V_d of a sphere with diameter 1:

$$\int d\hat{\boldsymbol{\sigma}}\,\Theta(\hat{\boldsymbol{\sigma}}\cdot\hat{\boldsymbol{v}}_{12})(\hat{\boldsymbol{\sigma}}\cdot\hat{\boldsymbol{v}}_{12})^2=\frac{\pi^{d/2}}{d\Gamma(d/2)}=2^{d-1}V_d, \tag{B7}$$

where Γ is the Euler function and it is understood that $\hat{\boldsymbol{v}}_{12}$ denotes an arbitrary unit vector in Eq. (B7). The volume V_d is itself related to the packing fraction η through $\eta=\rho V_d\langle\sigma^d\rangle$. From the definition of kinetic temperatures $\int v^2\varphi_i(\boldsymbol{v})d\boldsymbol{v}=dT_i/m_i$, we get

$$P^{\mathrm{ex}}=\rho\eta 2^{d-2}\sum_{i,j}\chi_{ij}x_i x_j\frac{m_i m_j}{m_i+m_j}(1+\alpha_{ij})\left(\frac{T_i}{m_i}+\frac{T_j}{m_j}\right)\frac{\sigma_{ij}^d}{\langle\sigma^d\rangle}, \tag{B8}$$

from which we deduce the equation of state (4). In this last step, no approximation (e.g., Gaussian, etc.) is made concerning φ_i. On the other hand, the computation of any other moment $(\hat{\boldsymbol{\sigma}}\cdot\boldsymbol{v}_{12})^p$ than $p=2$ requires the detailed knowledge of the velocity distributions [25]. It is also noteworthy that the decoupling of velocities $\boldsymbol{v}_1$ and $\boldsymbol{v}_2$ in Eq. (B6) is a specific property of the momentum transfer, which significantly simplifies the calculation.

APPENDIX C: HYDRODYNAMICS

In this appendix, we recall the hydrodynamical approach considered by Brey *et al.* [1], and adapt it to the case of energy injection at both boundaries $y=0$ and $y=L$. The situation investigated in Ref. [1] is that of a vibrating wall at $y=0$ and a reflecting wall at $y=L$, so that the temperature and density gradients vanish at $y=L$. In our no-flow configuration with two vibrating walls, the gradients vanish by symmetry in the middle of the cell ($y=L/2$), so that restricting to $y\in[0,L/2]$ allows us to use directly the expressions derived in Ref. [1] (which amounts to the formal identification $y\to 2y$ and $N\to 2N$). For completeness and clarity, we will, however, adapt the argument to our geometry.

In the case of a stationary system without macroscopic velocity flow, the hydrodynamic equations reduce to

$$\boldsymbol{\nabla}\cdot\boldsymbol{P}=0, \tag{C1}$$

$$\frac{2}{\rho d}\boldsymbol{\nabla}\cdot\boldsymbol{q}+T\zeta=0. \tag{C2}$$

Here $\boldsymbol{P}$ is the pressure tensor, $\boldsymbol{q}$ is the heat flux, and ζ the cooling rate due to the collisional energy dissipation. In the Navier-Stokes approximation for a low-density gas described by the Boltzmann equation modified to account for the inelastic nature of collisions [40],

$$\boldsymbol{P}=P\boldsymbol{I}, \tag{C3}$$

$$\boldsymbol{q}=-\kappa\boldsymbol{\nabla}T-\mu\boldsymbol{\nabla}\rho, \tag{C4}$$

where P is the ideal gas pressure $P=\rho T$. The explicit expressions of the heat conductivity κ, the transport coefficient μ, and cooling rate ζ may be found in Ref. [1]. The important ingredient is that μ is proportional to $T^{3/2}/\rho$ and κ to $\sqrt{T}$, while $\zeta\propto p/\sqrt{T}$, with coefficients depending on the inelasticity α.

The system is considered homogeneous in the x direction, so that only gradients along the y direction are taken into account. We emphasize that the ideal gas equation of state ($P=\rho T$) is assumed, and this simplification is an important ingredient in the following derivation. The previous equations then reduce to

$$\frac{\partial P}{\partial y}=0, \tag{C5}$$

$$\frac{2A(\alpha)}{d\rho}\frac{\partial}{\partial y}\left(\sqrt{T}\,\frac{\partial T}{\partial y}\right)-p\sqrt{T}=0. \tag{C6}$$

In order to simplify the equation on the temperature, it is convenient to introduce a new variable ξ, defined by

$$d\xi=\sqrt{a(\alpha)}\,\frac{dy}{\lambda(y)}=C\sigma^{d-1}\sqrt{a(\alpha)}\rho(y)dy, \tag{C7}$$

where $\lambda(y)=[C\sigma^{d-1}\rho(y)]^{-1}$ is the mean free path ($C=2\sqrt{2}$ for $d=2$), and $a(\alpha)$ includes all the dependence in α. Equation (C6) now reads

$$\frac{\partial^2}{\partial\xi^2}\sqrt{T}=\sqrt{T}. \tag{C8}$$

The variable ξ takes values between 0 and ξ_m, with $\xi_m\propto N$. Then $\sqrt{T}=A\exp(-\xi)+B\exp(\xi)$, where A and B depend on the boundary conditions. In the case of two vibrating walls, the solution is symmetric with respect to $y=L/2$ (or $\xi=\xi_m/2$). With $T(0)=T(\xi_m)=T_0$, one obtains

$$T(\xi)=\frac{T_0}{\sinh^2\xi_m}[\sinh(\xi_m-\xi)+\sinh\xi]^2. \tag{C9}$$

It is possible to integrate $d\xi=C\sigma^{d-1}\sqrt{a(\alpha)}n(y)dy=C\sigma^{d-1}\sqrt{a(\alpha)}p\,dy/T(y)$ to obtain $y(\xi)$ and P:

$$P=\frac{T_0}{2C\sigma^{d-1}L\sqrt{a(\alpha)}\cosh^2\frac{\xi_m}{2}}\,(\xi_m+\sinh\xi_m), \quad \text{(C10)}$$

$$\frac{y}{L}=\frac{\xi+\sinh\xi\cosh(\xi_m-\xi)}{\xi_m+\sinh\xi_m}. \quad \text{(C11)}$$

Those equations are the same as for the case of one vibrating wall [1], but with $\xi_m\to 2\xi_m$ and $L\to 2L$, as expected on the basis on the symmetry argument proposed above. It is possible to invert $T(\xi)$ and therefore to obtain the profiles $y(T)$ (two symmetric branches):

$$\xi=\frac{\xi_m}{2}\pm\cosh^{-1}\left(\sqrt{\frac{T}{T_0}}\cosh\frac{\xi_m}{2}\right), \quad \text{(C12)}$$

$$\frac{y}{L}=\frac{\xi+\sinh\xi\cosh(\xi_m-\xi)}{\xi_m+\sinh\xi_m}. \quad \text{(C13)}$$

[1] J.J. Brey, M.J. Ruiz-Montero, and F. Moreno, Phys. Rev. E **62**, 5339 (2000).
[2] J.J. Brey, M.J. Ruiz-Montero, and F. Moreno, Phys. Rev. E **63**, 061305 (2001).
[3] A. Prevost, D.A. Egolf, and J.S. Urbach, Phys. Rev. Lett. **89**, 084301 (2002).
[4] I. Goldhirsch and G. Zanetti, Phys. Rev. Lett. **70**, 1619 (1993).
[5] L.P. Kadanoff, Rev. Mod. Phys. **71**, 435 (1999).
[6] K. Feitosa and N. Menon, Phys. Rev. Lett. **88**, 198301 (2002).
[7] F. Rouyer and N. Menon, Phys. Rev. Lett. **85**, 3676 (2000).
[8] F. Rouyer and N. Menon (unpublished).
[9] K. Feitosa and N. Menon (private communication).
[10] A. Barrat, E. Trizac, and J.N. Fuchs, Eur. Phys. J. E **5**, 161 (2001).
[11] A. Barrat and E. Trizac, e-print cond-mat/0202297.
[12] S. Luding, Phys. Rev. E **52**, 4442 (1995).
[13] W. Losert, D.G.W. Cooper, J. Delour, A. Kudrolli, and J.P. Gollub, Chaos **9**, 682 (1999).
[14] R.D. Wildman and D.J. Parker, Phys. Rev. Lett. **88**, 064301 (2002).
[15] Y. Limon Duparcmeur, Ph.D., thesis, l'Université de Rennes I, 1996 (unpublished).
[16] V. Garzó and J. Dufty, Phys. Rev. E **60**, 5706 (1999).
[17] A. Barrat and E. Trizac, Granular Matter **4**, 57 (2002).
[18] J.M. Montanero and V. Garzó, Granular Matter **4**, 17 (2002).
[19] R. Clelland and C.M. Hrenya, Phys. Rev. E **65**, 031301 (2002).
[20] S.R. Dahl, C. Hrenya, V. Garzó, and J.W. Dufty, Phys. Rev. E **66**, 041301 (2002).
[21] J.M. Montanero and V. Garzó, e-print cond-mat/0201175.
[22] U. Marini Bettolo Marconi and A. Puglisi, Phys. Rev. E **65**, 051305 (2002); **66**, 011301 (2002).
[23] R. Pagnani, U.M. Bettolo Marconi, and A. Puglisi, e-print cond-mat/0205619.
[24] A. Santos, S.B. Yuste, and M. López de Haro, Mol. Phys. **96**, 1 (1999).
[25] I. Pagonabarraga, E. Trizac, T.P.C. van Noije, and M.H. Ernst, Phys. Rev. E **65**, 011303 (2002).
[26] J. Zhang, R. Blaak, E. Trizac, J.A. Cuesta, and D. Frenkel, J. Chem. Phys. **110**, 5318 (1999).
[27] J.T. Willits and B.Ö. Arnarson, Phys. Fluids **11**, 3116 (1999).
[28] S. McNamara and J.-L. Barrat, Phys. Rev. E **55**, 7767 (1997).
[29] E.L. Grossman, T. Zhou, and E. Ben-Naim, Phys. Rev. E **55**, 4200 (1997).
[30] K. Helal, T. Biben, and J.-P. Hansen, Physica A **240**, 361 (1997).
[31] D. Henderson, Mol. Phys. **30**, 971 (1975).
[32] The hydrodynamic theory of Ref. [1] predicts the value of ξ_m, which depends on α and is proportional to N. Since the hypothesis of Ref. [1] (isotropic pressure given by the ideal equation of state) is not verified in our simulations, we consider ξ_m as a fitting parameter; the corresponding values are close to the predictions of Brey *et al.*, [1] (with a difference of less than 10%).
[33] J.J. Breg and M.J. Ruiz-Montero, e-print cond-mat/0210158.
[34] I.S. Aranson and J.S. Olafsen, e-print cond-mat/0110607.
[35] The numerical data shown in Fig. 8 display a peak at $\alpha_{1d}=\alpha$, i.e., at the original value of the restitution coefficient in the initial hard-disc model. This peak does not seem to be present in the experimental data either due to a lack of statistics, or because the experimentally measured normal restitution coefficient depends slightly on the collision parameters (relative velocity, impact parameter, etc.), leading to a smoothening of this peak.
[36] V. Garzó and J.W. Dufty, Phys. Fluids **14**, 1476 (2002).
[37] T. Biben, Ph.A. Martin, and J. Piasecki, Physica A **310**, 308 (2002).
[38] T.P.C. van Noije, M.H. Ernst, E. Trizac, and I. Pagonabarraga, Phys. Rev. E **59**, 4326 (1999).
[39] M.P. Allen and D.J. Tildesley, *Computer Simulation of Liquids* (Clarendon Press, Oxford, 1987).
[40] J.J. Brey, J.W. Dufty, and A. Santos, J. Stat. Phys. **87**, 1051 (1997).